Cavity-Enhanced Linear Dichroism in a van der Waals Antiferromagnet

Huiqin Zhang,[1,‖] Zhuoliang Ni,[2,‖], Christopher E. Stevens[3], Aofeng Bai,[4] Frank Peiris,[4] Joshua R. Hendrickson[3], Liang Wu,[2] Deep Jariwala[1]*

[1] *Department of Electrical and Systems Engineering, University of Pennsylvania, Philadelphia, PA 19104, USA*

[2] *Department of Physics and Astronomy, University of Pennsylvania, Philadelphia, PA 19104, USA*

[3] *Air Force Research Laboratory, Sensors Directorate, Wright-Patterson Air Force Base, Ohio, 45433, USA*

[4] *Department of Physics, Kenyon College, Gambier, OH 43022, USA*

[‖] *These authors contributed equally: Huiqin Zhang, Zhuoliang Ni*

[*]Corresponding author: dmj@seas.upenn.edu

Abstract:

Optical birefringence is a fundamental optical property of crystals widely used for filtering and beam splitting of photons. Birefringent crystals concurrently possess the property of linear dichroism (LD) that allows asymmetric propagation or attenuation of light with two different polarizations. This property of LD has been widely studied from small molecules to polymers and crystals but has rarely been engineered per will. Here, we use the newly discovered spin-charge coupling in van der Waals antiferromagnetic (AFM) insulator $FePS_3$ to induce large in-plane optical anisotropy and consequently LD. We report that the LD in this AFM insulator is tunable both spectrally and magnitude wise as a function of cavity coupling. We demonstrate near-unity LD in the visible-near infrared range in cavity-coupled $FePS_3$ crystals and derive its dispersion as a function of cavity length and $FePS_3$ thickness. Our results hold wide implications for use of cavity tuned LD as a diagnostic probe for strongly correlated quantum materials as well as opens new opportunities for miniaturized, on-chip beam-splitters and tunable filters.

Introduction:

Optical anisotropy plays a crucial role in light manipulation for photonic and optoelectronic applications. Although giant out-of-plane optical anisotropy has been recently observed in the visible to mid-infrared wavelength range in perovskite chalcogenides, h-BN crystals and Mo, W chalcogenides[1], the in-plane optical anisotropy has been scarcely explored in low-dimensional van der Waals crystals. This has inspired an ongoing search for giant in-plane optical anisotropy among natural and artificial materials. To achieve in-plane anisotropy a material must possess some asymmetry in structural or electronic order along one direction. Often, this is achieved via anisotropic, one-dimensional (1D) structure of the material itself such as in liquid crystals or polymers[2] or carbon nanotubes. An effective way to quantify this anisotropy is via means of linearly polarized light spectroscopy often used to obtain linear dichroism (LD, the difference in reflected light intensities along two different polarizations)[1] or birefringence (the difference in refractive indices (Δ n) along two different polarizations), which represent a measure of anisotropic optical response. The property of LD has been very useful in producing versatile optical components[3, 4], including polarizers, wave plates, mirrors, and phase-matching elements. Despite

its great fundamental importance and technological significance, LD and in-plane LD in novel materials is rarely studied systematically, and further, even little has been known about tuning or engineering LD in low-dimensional optical materials. Among known in-plane anisotropic materials such as Black Phosphorous (BP) and ReS_2 LD has been recently measured with magnitudes of ~ 20% to 40%[5, 6] which primarily emanates from the in-plane asymmetry of atomic arrangements or crystal structure. However, these are static values and no investigations on engineering/tuning them have been reported thus far. A notable approach to tune/engineer optical anisotropy involves the use of artificially designed metamaterials and metasurfaces which comprise of patterned nanostructures and have been shown to exhibit large birefringence values[7]. Therefore, an in-depth study of LD and birefringence, particularly the ability to tune and enhance LD, is notably lacking. This ability to tune the LD would be particularly vital for wavelength tunable beam-splitters, waveguides and detectors.

The recent emergence of van der Waals chalcogenides with long-range magnetic order offer a unique opportunity in tuning light-matter interactions as a function of magnetic phase transitions or ordering. Magnetic phase transitions can induce spin-charge couplings that can result in breaking the symmetry of optical response in-plane leading to observation of LD. Magneto-optical effects such as magneto-optical Kerr effect (MOKE)[8, 9] are commonly used to detect such magnetic phase transitions and also spin configurations or ordering in ferromagnets. As compared to ferromagnets, however, the detection of antiferromagnetism (AFM) is much more difficult due to the lack of a net magnetic moment. Prior works have used neutron scattering[10, 11], Raman spectroscopy[12, 13, 14, 15] and second harmonic generation[16, 17, 18] to detect the symmetry of spin ordering in antiferromagnets(AFM), based on the expansion of the unit cell, magnetoelastic coupling, and inversion symmetry breaking, respectively. Here we show that in van der Waals AFM insulator $FePS_3$ a strong spin-charge coupling can induce large in-plane anisotropy leading to extraordinarily high LD values. These LD values can be further tuned by coupling them with a simple optical cavity medium which results in enhancement of the LD to near-unity values. In addition, the tuning of the cavity further allows spectral tuning of this large LD response. Our results suggest that van der Waals AFM semiconductors and insulators are outstanding candidates for the tuning and amplification of in plane LD in the visible to NIR range and open the door to novel, multi-spectral, miniature nanophotonic components by virtue of spin-charge coupling phenomena.

Results:

We report the observation of near-unity, tunable and cavity-enhanced linear dichroism in a broad-band visible-NIR region of the spectrum in thin layers of vdW AFM material $FePS_3$. $FePS_3$ belongs to a class of transition metal phosphorous trichalcogenides (MPX_3, M: Fe, Mn, Ni and X: S, Se), which are van der Waals AFM insulator materials with bandgap ranging from 1.3eV to 3.5eV[12, 13, 19, 20, 21]. Within individual $FePS_3$ layers, Fe atoms are arranged in a honeycomb lattice structure. The spins pointing out of plane along a chosen row of Fe atoms aligned in the zigzag direction (shown along the x-axis) are opposite to the spins in the adjacent spin chain of Fe atoms (Fig. 1a, the in-plane structure), forming a zigzag AFM order[22]. The blue and red Fe atoms are aligned at +z and -z direction, respectively. The interlayer coupling between adjacent layers is AFM, as shown in figure 1.a (out-of-plane structure). Raman spectroscopy[12] and magnetic susceptibility[23] measurements from literature precedent have shown that the Néel temperature is ~ 118 K in bulk

$FePS_3$. Below Néel temperature, the strong spin-charge correlation results in high optical anisotropy which is locked into the zigzag direction of $FePS_3$ crystal.[24]

To demonstrate this, linearly polarized optical reflectance measurements were performed on multilayer $FePS_3$, directly exfoliated on a Si/SiO_2 substrate (figure 1.b, SiO_2: 90nm thickness). The samples show varying colors with varying thicknesses suggesting strong optical interference effects. We use a polarizer placed in the reflected light path to the detector to detect the polarized reflectance and the linear dichroism (LD) from the sample (figure 1.c). The axes along which in-plane anisotropy is induced are also shown in figure 1.b. Within this multilayer $FePS_3$ structure, the LD can be enhanced from the cavities formed vertically inside the material which is indicated by the orange oval marked in figure 1.c.

We define LD as $\frac{R_\perp - R_\parallel}{R_\perp + R_\parallel}$, where $R_\parallel$ ($R_\perp$) is the peak intensity of horizontally (vertically) polarized optical reflection (see methods)[25]. The above expression can also be understood as difference in reflection between the two axes divided by total reflect unpolarized reflection. Figure 1.d shows the high degree of optical anisotropy with LD up to 98.6% for measurements performed at 30 K at 751 nm wavelength. The LD is observed to be a strong function of the temperature as shown in Figure 1.e. The transition of LD from ~10% to ~100 % begins at 130 K and is complete by 110 K coinciding with a precipitous drop at the Néel temperature (T_C ~118 K). The LD magnitude approaches the highest level of 98.6% below Néel temperature, following the antiferromagnetic phase transition. This temperature dependence is similar to prior reports on temperature dependent Raman spectroscopy[12, 13] and magnetic susceptibility[23] which indicates spin-charge coupling due to the AFM ordering. This further supports our evidence of LD induced by the AFM transition and spin ordering along the zigzag crystallographic direction.

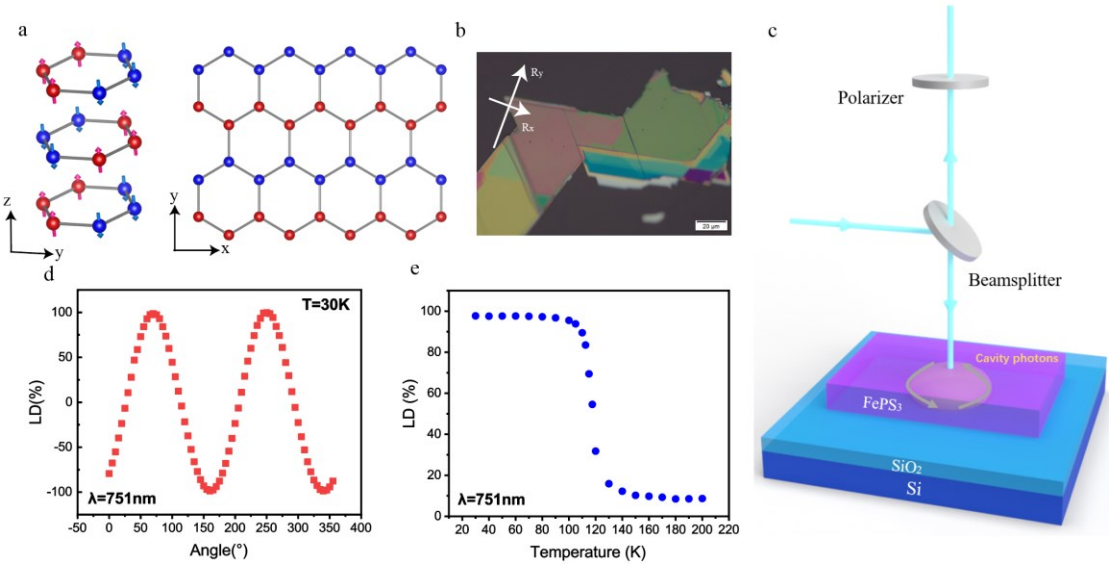

Figure 1 Optical in-plane anisotropic behavior in AFM van der Waals $FePS_3$. a. Schematic of zigzag AFM order in a single layer $FePS_3$ (right) and in multilayer stacks (left). The blue and red atoms represent the Fe atoms with spins in opposite directions. b. Optical image of exfoliated $FePS_3$ on Si/SiO_2 substrate indicating the crystallographic axes (x and y corresponding to the ZZ and AC direction respectively). c. Schematic of the experimental setup of the linearly polarized optical reflectance microscope used to measure the multilayer $FePS_3$. The cavity photons (indicated by an

orange oval) form inside the layered material. d. $FePS_3$ LD intensity as a function of linear polarization angle. Data is acquired at 30K with an incident wavelength at 751nm, indicating a near-unity LD (98.4%). The linear dichroism at 751 nm of $FePS_3$ multilayer sample as a function of temperature showing T_C=118 K.

To further understand the nature of this optical response, we perform polarized spectral reflectance in the VIS-NIR range and estimate the LD spectrum. Figure 2.a shows an optical micrograph and the corresponding AFM topography of the $FePS_3$ crystal sample. The AFM line cut shows the step edge of the sample corresponding to a thickness of 268nm. As shown in the polarization angle-dependent reflectance spectra (figure 2.b), the extinction (reflectance) is highly dependent on the incident light polarization and consequently also the LD (Figure 2c). Several resonant absorption (reflection) peaks are visible with values corresponding to near-unity absorption, particularly at ~750 nm. These resonant reflectance peaks suggest that the reflected light is strongly attenuated in the layered material due to the thin film interference effect[26]. Briefly, a film with a thickness of $k\frac{\lambda}{2n_{eff}}$ (k is an integer as an order number, λ is the incident light wavelength, n_{eff} is the effective refractive index of the combined group of several vertically stacked thin films, used to define occurrence of the cavity mode due to phase matching condition.) would form an optical cavity where light (photons) of specific wavelengths will be trapped inside the film and thereby result in enhancement of the absorption[27, 28]. Hence, the resonant absorption (reflectance) peaks in figure 2.b correspond to different orders of Fabry-Perot cavity mode resonances. The high anisotropy is also observed in the polarized reflectance spectra. The absorption resonances significantly vary at different polarized angles illustrating the in-plane birefringence (Δn) of $FePS_3$ since the cavity resonance mode is highly dependent on n_{eff}. The lattice anisotropy axes can be determined by plotting the polar plot of the reflectance intensities which also depends on the wavelength, as is shown in figure 2.c. The polarization angle of 340° (70°) corresponds to the long (short) axis of lattice anisotropy. We also perform temperature dependence reflectance measurements along the long (340°, figure 2.d) and short axes (70°, figure 2.e). It is evident from these reflectance measurements that the cavity resonance at 765 nm blue-shifts (red-shifts) while the cavity resonance at 523 nm red-shifts (blue-shifts) at 340° (70°) polarized angle as $FePS_3$ goes through AFM ordering below its transition temperature. This indicates that the birefringence originates from the AFM order, and the birefringence is also spectrally dispersive. The reflectance of at 751 nm (862 nm) is the highest (lowest) at 340° polarization angle while it is lowest (highest) at 70° polarization. Figure 2.f shows the temperature dependence of LD spectrum as derived from Figure 2.b. It is evident from the plot that the LD intensity variations extend broadly in the visible and NIR spectrum. Multiple peaks are observed in the LD spectrum corresponding to multiple cavity modes formed by the crystal in the reflectance spectrum in figure 2.b. The largest LD peak reaches up to 98.6% corresponding to the near-unity cavity-resonant absorption peak at 751 nm and the second-largest LD reaches to 80.0% corresponding to absorption peak at 862 nm in the reflectance spectrum. More LD peaks at shorter wavelengths show the lower intensity and correspond to the higher-order resonant-cavity modes. The absorption losses at these cavity-resonances correspond to absorption in both the $FePS_3$ as well as the underlying Si/SiO_2. The temperature dependence of LD spectra shows a drastic reduction in the magnitude of the LD above 118 K, matching well with the Néel temperature of

$FePS_3$. More reflectance and LD measurements have been performed on multiple samples with varying thicknesses ranging from 80 nm to 270 nm shown in Supplementary Information. The cavity-enhanced LD are observed similarly in various flakes, and multiple LD peaks are also observed at different wavelength ranges due to the various thicknesses of the samples (See supporting information S1 for more details).

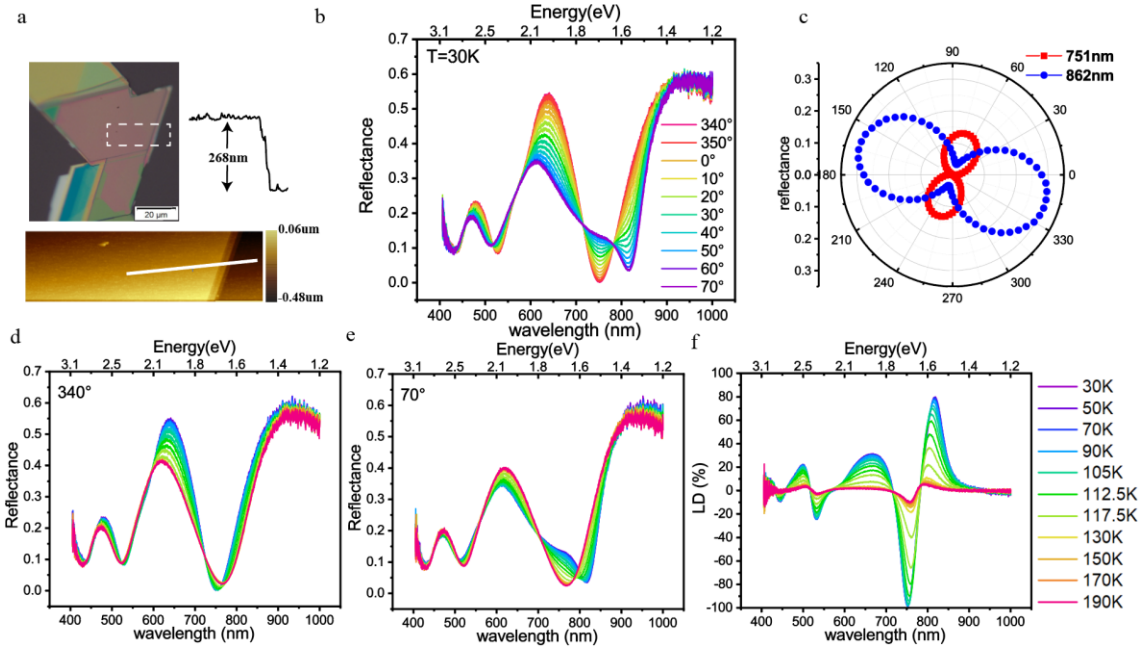

Figure 2 Linear dichroism spectrum of $FePS_3$. a. Optical image of the exfoliated $FePS_3$ crystal sample. Inset shows an atomic force topography image of the area enclosed by the dashed rectangle. Line cut (white line) and the corresponding height plot indicates the sample thickness as ~268 nm. b. Polarization angle dependence of reflectance intensity spectra measured at 30 K with a step of 5 degrees polarization rotation from 340-70 degrees. c. Polar plot of $FePS_3$ reflectance intensity as a function of linear polarization angle (steps of 5 degrees) at a specific wavelength of 751 nm (red) and 862 nm (blue) respectively. The large anisotropy of in-plane crystallographic axes is evident. d,e Temperature dependence of the reflectance intensity spectra at polarization angles of 340° (d) and 70°(e). f. Temperature dependence (30 K to 200 K) of the linear dichroism (LD) spectrum.

To better understand the cavity-enhanced LD of this structure and its thickness dependence, we perform electromagnetic wave calculations using the transfer matrix method (TMM) to estimate the thickness-dependent reflectance and the LD intensity. To make a correct estimate from TMM calculations we measure the dielectric function of $FePS_3$ by spectroscopic ellipsometry (See Supplementary Information 2 for the fitting details). The ellipsometry results are based on a large bulk crystal (~1mm size) measured at room temperature where the original refractive index n and k are derived without AFM ordering, which are primarily isotropic. To derive the birefringence of $FePS_3$ with AFM ordering, a low temperature polarized reflectance measurement with normal incident light is performed on the bulk crystals (with 1 mm thicknesses, thereby avoiding any cavity enhancement effects) and the LD spectrum for the same is shown in Figure 3.a.

The refractive index from the two anisotropic axes n1 and n2 can be derived from the reflectance data (Supplementary Information 3) by applying Fresnel equation,

$$R = \left|\frac{\tilde{n} - 1}{\tilde{n} + 1}\right|^2$$

here $\tilde{n} = n + ik$ is a complex value.

Here the reflectance measurement is just with a normal incident light without having a s and p wave polarization difference. Therefore, the imaginary part of refractive index (extinction coefficient: k) cannot be derived. In this case, we derive the n1 and n2 without considering the imaginary part. This means we assume there is no change in extinction coefficient for two anisotropic axes. (Δ k=0) From (1), we can get n1 and n2 with all real values:

$$n_1 = \frac{1 + \sqrt{R_1}}{1 - \sqrt{R_1}}$$

$$n_2 = \frac{1 + \sqrt{R_2}}{1 - \sqrt{R_2}}$$

And the birefringence is derived: Δ n=n1-n2. The exact calculation details on the estimation and assumptions of the birefringence spectra are provided in Supplementary Information 3. This quantification at every wavelength result in the estimation of the birefringence (Δn) spectrum (figure 3.b). The birefringence ranges from -0.2 to 0.075 depending on the wavelength. The birefringence spectrum shows an interesting feature of crossing over from positive values below 650 nm to negative values at above 650 nm, indicating the presence of an electronic band resonance in $FePS_3$ [29]. This behavior also explains the opposite directions of shifts in cavity-resonance peaks at 523 nm and 765 nm position respectively in the reflectance spectra shown in Figure 2.d & e. The real part of the refractive index (n) in the visible range as estimated from ellipsometry at room temperature (without AFM ordering) is also shown in the inset of Figure 3.b. When applying the dielectric function of the two anisotropic axes for TMM calculations, we want to make it closer to the real values measured from ellipsometry data. Therefore, instead of directly applying n1 and n2, we normalize the data with $\left(n + \frac{\Delta n}{2}, k\right)$, $\left(n - \frac{\Delta n}{2}, k\right)$ for the refractive index (including extinction coefficients) of two anisotropic axes. Here, n and k are original isotropic refractive index derived from the ellipsometry data at room temperature and the Δ n is the birefringence derived from the reflectance measurements at low temperature. (See Supplementary Information 4 for TMM calculation details) Figure 3.c shows the experimental LD spectra of $FePS_3$ for various thicknesses. The corresponding simulated LD spectra (Figure 3.d) show a close qualitative match in terms of resonances and features observed in the experimental spectra as indicated by the corresponding labels. This cavity model along with our simulations also explains and proves the change of polarization axes from positive to negative at different wavelengths. There is, however, some quantitative mismatch between the simulation and the experimental result due to two main reasons: One, the estimation of the birefringence is not perfect in this case since we are not considering difference in extinction coefficients (Δ k) for the two anisotropic axes. This will induce an intensity mismatch from simulation to experiments. Second, the AFM domains of $FePS_3$ may not be the same size and ideally matched in each FePS3 unit layer, which means the sampled thickness in the experiment may not be the ideal thickness for the calculations. To further

understand the nature of these resonances, we also check the electric field distributions along the cross-section of $FePS_3$ crystal, i.e. in the plane normal to the basal plane of the crystal, as shown in figure 3.e. For thin-film interference, the cavity resonance occurs at $d = k\frac{\lambda}{2n_{eff}}$ (where k is the order of the mode) which is the approximate value of the resonant wavelength at the specific thickness (Figure 3.c &d). The peaks in LD are labeled with an upright triangle, a square and a star symbols (Figures 3.c-e) and correspond to first, second and third-order cavity modes respectively formed inside $FePS_3$ crystal (in 3.e). The field profiles again verify that the LD is enhanced due to the cavity modes.

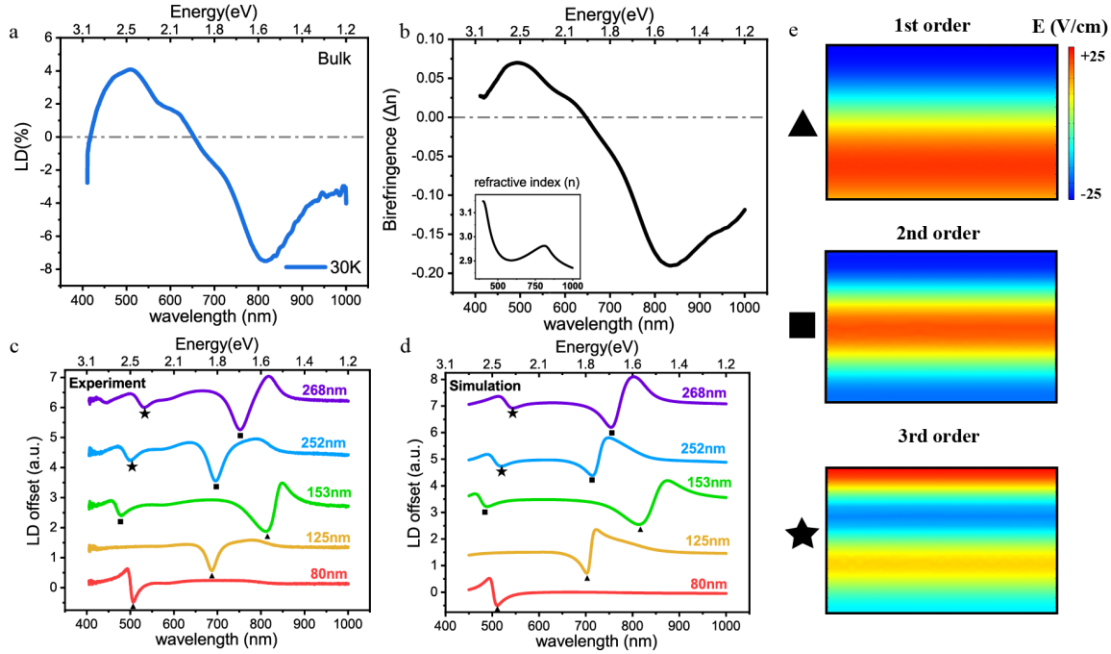

Figure 3 Simulation model of cavity enhanced multilayer $FePS_3$. a. LD spectrum of bulk (> 100 microns thickness) $FePS_3$ crystal measured at 30 K. b. The birefringence spectrum at 30 K calculated from (a). The spectrum shows a wavelength dependent birefringence of $FePS_3$, indicating a positive Δn below 650 nm which transitions to a negative Δn above 650 nm. The inset is refractive index (real part) of $FePS_3$ measured via spectroscopic ellipsometry method (298 K). c. Experimental LD spectra for specific $FePS_3$ thicknesses of 80 nm, 125 nm, 153 nm, 252 nm, 268 nm. All measurements were performed at 30 K. d. Transfer matrix calculated LD spectra for the same thicknesses as in (c). The LD peaks match well in terms of qualitative shape and spectral positions. e. Electric-Field profiles of the Fabry-Perot cavity-mode resonance peaks labelled in (c) and (d). The triangles indicate the first-order cavity mode, while the squares and the stars indicate the second-order and third-order cavity modes respectively.

Given that the resonance magnitude and spectral position in LD is tunable as a function of $FePS_3$ thickness, this system provides a unique opportunity in exploring tunability of the LD spectrum. This can be done in two ways. Figure 4.a shows the approaches adopted here to tune the optical cavity sizes using both internal and external cavity media. For a fixed thickness of the substrate layer (i.e. bulk Si with some fixed SiO_2 thickness on top), if the thickness of $FePS_3$ is much smaller (4.a (i)) than the incident wavelength, then the light will pass through $FePS_3$, leaving the

material with minimal loss. Likewise, if the thickness is much larger (4.a (ii)) than the light will be fully absorbed or reflected before reaching the bottom-most layers of $FePS_3$. In neither of the two cases will the $FePS_3$ layers form and support cavity modes. Only when the thickness of $FePS_3$ is at a comparable level to that of the incident light wavelength (4.a (iii)), the material will be capable of supporting a stable cavity for the photons, forming a standing wave inside it. In this case, the photons are trapped in the $FePS_3$, which enhances the light-matter interaction and thus the LD. Similarly, one can achieve the spectral tuning of the LD peaks by changing the size of external cavities (SiO_2, 4.a (iv)). The detailed electric field profiles of the cavity resonances formed by the internal cavity ($FePS_3$) and external cavity (SiO_2) are shown in comparison in Supplementary Information 5. First, by sweeping the thickness of $FePS_3$, one can simply achieve the spectral tuning of the LD peaks by tuning the cavity size itself. Figure 4.b shows a color map of LD spectra as a function of $FePS_3$ thickness with the LD magnitude and sign (red positive, blue negative) shown on the color scale. The stars, squares and triangular symbols correspond to the experimentally observed LD peaks in figure 3(c). In this map, the linearly dispersive branches of the LD resonances correspond to the first, second and third-order Fabry-Perot cavity modes respectively. The lowest order modes show the strongest LD contrast while the higher order modes show weaker contrast. The color plot further shows that the desired thickness range for $FePS_3$ crystals on 90 nm SiO_2/Si is ~270 nm for observation of maximum magnitude of LD under reflectance in the visible wavelengths range. The second way of tuning the LD is to tune the substrate SiO_2 thickness. For a fixed layer thickness of $FePS_3$ below 50 nm where the material is too thin to form any internal cavity to support a mode, we can use the external cavity (SiO_2) to enhance the absorption and LD of $FePS_3$ as seen in Figure 4.c. Here, the thickness of $FePS_3$ layer is fixed at ~15 nm. Multiple orders of LD peak branches are observed and the symbols in the spectral map once again denote the experimental LD peak positions of 1^{st} order (triangles), 2^{nd} order (square) and 3^{rd} order (star) resonances. The corresponding full experimental spectra (line-plots) are shown in Supplementary Information 6. Several $FePS_3$ crystal samples with roughly the same thickness (~15 nm) when measured on Si substrates with different SiO_2 thicknesses (50 nm, 90 nm, 280 nm) show shifting of the LD resonance peak (Figure 4.c). This observation further verifies that the LD response is tunable by changing the optical cavity sizes. Further, we also implement a better closed optical cavity to enhance the absorption and LD further in monolayer systems $FePS_3$ by calculation. The referenced model with Au/Al_2O_3 layers as mirror and dielectric layers encapsulating monolayer $FePS_3$ is shown in Supplementary Information 7. The closed optical cavity with metallic mirrors and Al_2O_3 on both sides can strongly couple the cavity photons into even a monolayer material with an enhanced absorption to near-unity level. By controlling the size of the applied optical cavity, the monolayer $FePS_3$ can reach a near-unity absorption at a specific wavelength range. As a result, the near-unity LD can be generated due to the large absorption peak even with a small birefringence in monolayers. This demonstrates that the enhancement of LD is possible beyond monolayer limit.

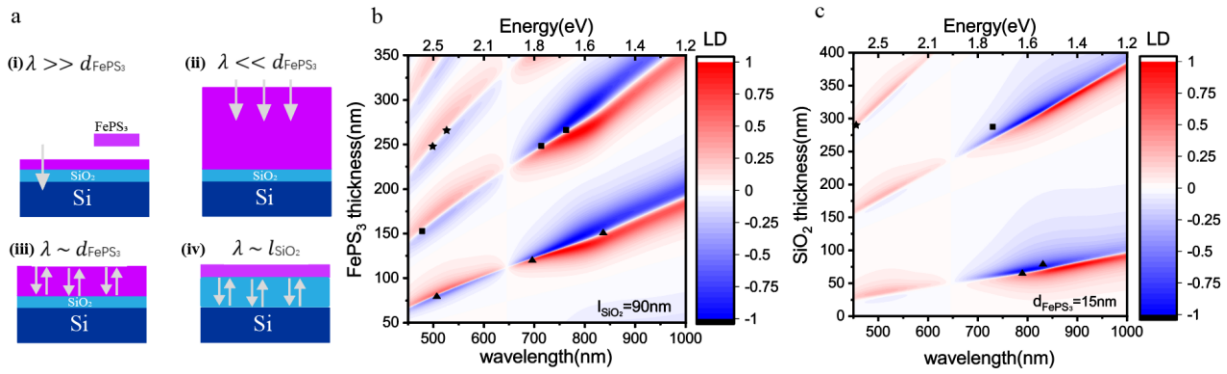

Figure 4 Spectral tuning of LD enhancement by tuning cavity sizes. a. Schematic illustration of internal and external Fabry-Perot cavity mode formation in $Si/SiO_2/FePS_3$ stacks with varying thicknesses of $FePS_3$ (internal cavity) and SiO_2 (external cavity). Resonant enhancement of the LD signal is observed at the cavity modes. b. Calculated LD spectral color plot as a function of $FePS_3$ thicknesses. The color scale on the map indicates the magnitude of LD resonance (red positive, blue negative) induced by the internal cavity formed in $FePS_3$ which is tuned by changing the $FePS_3$ thickness. The black symbols correspond to the experimentally measured LD peaks from figure 3(c). c. Calculated LD spectral color plot as a function of varying dielectric layer SiO_2 thicknesses. The map indicates that the LD resonances in thin $FePS_3$ can be spectrally tuned by the external cavity formed by varying index between $Si/SiO_2/FePS3$ and can be tuned simply by changing the SiO_2 thickness upon keeping FePS3 thickness constant at a thin value. The black symbols correspond to the experimentally measured 1st order (triangle), 2nd order (square) and 3rd order (star) LD resonances, respectively.

Discussion and Outlook:

The experiments, calculations and results above have several important implications both at a fundamental level and in terms of potential for future applications. LD spectroscopy is a valuable technique in probing anisotropic spin structures in AFM materials. Since the optical anisotropy axis is locked to the zigzag direction in real space along which the spin chains are aligned, polarized LD can also serve as a probe in detecting or imaging AFM domains (Figure 5. a,b). The mapping results shows the randomly oriented AFM-zigzag domains on the same sample where the color denotes the orientation of LD and the length denotes the relative intensity of LD. The exact polarized LD results at several specific points from the thick samples with flatter surface is also shown in Supplementary Information 8. As compared to thicker samples which have limited LD orientations (Supplementary Information 8), more domain variations are seen in thinner samples (~20nm)(Figure 5.b) due to the unevenness of the sample and the external strain induced from the flexible PDMS substrate.[18] This demonstrates that the AFM-zigzag domains are tunable from external stimuli like strain and can be detected by virtue of spatially mapping LD.

Since the spin-charge coupling strongly manifests in the linear dichroism, the intrinsic birefringence of $FePS_3$ can be tuned in many different ways. The tunability of AFM-zigzag domains provides the platform for several potential applications as shown in Figure 5.c. First, the birefringence orientation can be tuned when the in-plane magnetic field (Figure 5.c.i) exceeds the spin flip transition to flip the AFM-zigzag domain state[30]. An out-of-plane external magnetic field can also

affect the intrinsic birefringence as shown in Supplementary Information 9. Second, the birefringence orientation can also be tuned through external strain (Figure 5.c.ii)[18]. The AFM Neel vectors are very sensitive to the external strain. Therefore, the direction of LD can be controlled by the competition of strain and original AFM order along zigzag direction. This is also illustrated from Figure 5.b with a randomly oriented LD directions originating from the randomly oriented external strain of an FePS3 flake exfoliated on poly dimethoxy silane (PDMS). Third, the birefringence tunability can also be controlled via various nanophotonic structures (Figure 5.c.iii). By tuning the AFM orders both in magnitude and orientations using different external stimuli, AFM insulators allow control of optical anisotropy of the medium in multiplexed ways opening new directions in nanophotonic design such as integration with Bragg Mirror based cavities and patterning of sub-wavelength resonators (Figure 5 c iii). The cavity-coupled enhancement of LD demonstrated in this work is an example of a simple fabrication free photonic structure. It is worth noting that the AFM-coupled LD of $FePS_3$ originates from a phase transition from a parametric phase to an AFM phase corresponding to a structural symmetry breaking. This will also pave the way for opportunities in tunable topological photonic metasurface comprised of AFM insulators. Further, the tunability of birefringence in antiferromagnets can also be expanded to include tunability applications via temperature control, gating control of monolayers, doping level in materials, etc. Finally, it is also worth noting that although the critical temperatures (Tc) of the van der Waals AFMs and FM are cryogenic, it is well known that the Tc can be elevated by doping[31, 32] and nanostructuring[33, 34] thereby making them more suitable for realistic applications.

In summary, the extremely high LD (98%) demonstrated in $FePS_3$ is among the largest in most two-dimensional anisotropic materials[5, 6, 35, 36] and makes it an attractive candidate for future anisotropic optical elements. In addition, the ability to tune the AFM-coupled birefringence in magnitude and orientation both spectrally and spatially by means varying external stimuli such as magnetic field, strain and artificial nanostructuring opens new opportunities in nanophotonic component design particularly as ultrathin and highly birefringent materials for on-chip filtering, beam splitting as well as non-linear optical components.

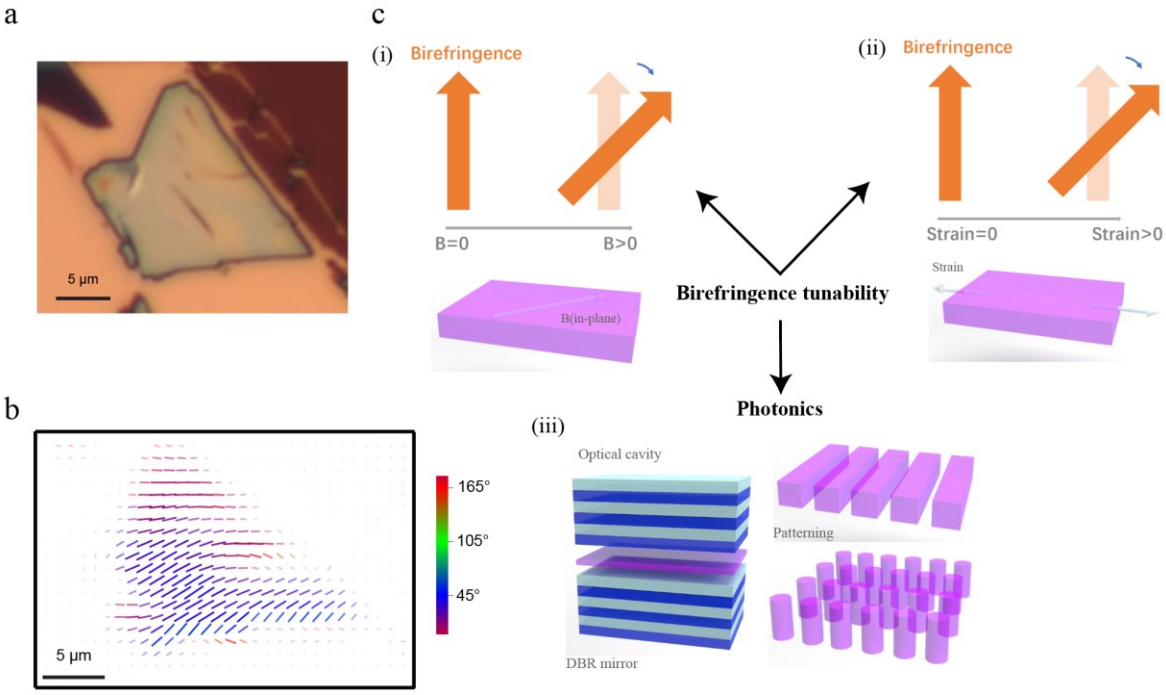

Figure 5 Linear dichroism mapping and potential applications for birefringence tunability. a. Optical image of an $FePS_3$ flake sample exfoliated on a PDMS. The sample is ~20 nm thickness. b. The LD mapping image corresponding to the sample in (a). The LD is measured by an incident single wavelength laser with 800 nm. Here, the color and the direction denote the LD orientation and the length denotes the relative intensity of LD. The mapping shows randomly oriented domains on the same single flake. c. Schematic designs for birefringence tunability for potential future applications. (i) Tunable birefringence from external in-plane magnetic field. (ii) Tunable birefringence from external strain. (iii) Tunable birefringence via cavity coupling and nanostructuring integrated nanophotonics.

Methods

Sample preparation

$FePS_3$ layers were mechanically exfoliated from bulk crystal (HQ-graphene) using Scotch Tape and transferred onto the Si/SiO_2 substrate with thermally grown oxide in a dry process. The Si/SiO_2 wafers with SiO_2 thicknesses of 50 nm, 90 nm and 280 nm, were commercially purchased. For sample thickness-dependent measurements, samples are transferred on the same substrate with SiO_2 thickness of 90 nm. For dielectric layer-dependent measurements, different $FePS_3$ crystal samples with the same thickness of ~15 nm were transferred onto the substrate with 50 nm, 90 nm, 280 nm SiO_2 thickness.

Reflectance measurement

The normalized reflectance intensity from 0 to 1 are all achieved by subtracting the background and normalizing with a reflectance intensity from a silver mirror.

$$R_{normalized} = \frac{R_{sample} - R_{background}}{R_{silver}}$$

Linear dichroism measurement

An unpolarized halogen light source (AvaLight-HAL) is focused on the sample by a 50X objective (Olympus SLMPLN 50X N.A.=0.35). The reflected light is analyzed by a linear polarizer and collected by a multi-mode optical fiber into a spectrometer with a charge-coupled device camera. The polarization-dependent LD spectrum is calculated by $\frac{R_\perp - R_\parallel}{R_\perp + R_\parallel}$, where $R_\perp$, $R_\parallel$ are the reflectance perpendicular and parallel to the polarization[25]. The sample was loaded in a helium-free cryostat for these measurements.

Ellipsometry

Ellipsometry spectra were obtained at three angles of incidence (65°, 70° and 75°) using a VASE ellipsometer (J.A. Woollam). Since the sample size was small, a focusing-optics module with a spot size of ~100 μm was attached to the instrument. Additionally, the instrument was equipped with an auto-retarder to monitor the depolarization caused mainly by non-specular reflections[37]. Scans with high depolarization values (~10% or higher) were discarded as they were harder to model, and scans with only low depolarization values were used obtain the dielectric function of the sample. More details of the dielectric function results are in Supplementary Information Part 2.

Magnetic-tunable LD measurement

The sample's LD magnetic field dependence was measured in an attoDRY2100 cryostation with the sample held at 30K. The magnetic field was swept from –9T to +9T in the Faraday geometry. White light was produced by a stabilized tungsten-halogen light source (ThorLabs, SLS201L) and focused onto the sample with a 0.82 NA in-situ microscope objective. The reflected light was sent through a Glan-Thompson linear polarizer, dispersed in a SpectraPro spectrometer (Princeton Instruments, SP-2750) and collected by a CCD camera (Princeton Instruments, 400 BR-excelon).

Calculations

All the calculations and simulations are done by the transfer matrix method. Details are discussed in Supplementary information Part 4.

Contributions

D.J., H.Z. and Z.N. conceived the project. H.Z. and Z.N. made the samples, performed linear polarized reflectance measurements, and atomic force microscopy characterization. H.Z. and Z.N. performed the calculation work. C.S and J.H performed magnetic-tunable linear dichroism measurements. F.P. and A.B performed the ellipsometry measurements. H.Z. analyzed and interpreted the optical spectroscopy and simulation data with help from Z.N. and D.J. H.Z. and D.J. wrote the paper with input from all co-authors. D.J. supervised the study.

Acknowledgements

D.J. acknowledges primary support for this work by the U.S. Army Research Office under contract number W911NF-19-1-0109. D.J. also acknowledges support from National Science Foundation (NSF) supported University of Pennsylvania Materials Research Science and Engineering Center (MRSEC) (DMR-1720530). H.Z. was supported by Vagelos Institute of Energy Science and Technology graduate fellowship. L.W. acknowledges support from the ARO under the Grants W911NF1910342 and W911NF2020166 and a seed grant from NSF supported University of Pennsylvania Materials Research Science and Engineering Center (MRSEC) (DMR-1720530). F.P. acknowledges support from Kenyon College and NSF grant DMR-2004812. JRH acknowledges support from the Air Force Office of Scientific Research (Program Manager Dr. Gernot Pomrenke) under award number FA9550-20RYCOR059. The authors acknowledge assistance from Jason Lynch for spectroscopic ellipsometry measurements.

Conflicts of interests: The authors declare no competing or conflicting interests.

References:

1. Ermolaev G, Grudinin D, Stebunov Y, Voronin K, Kravets V, Duan J*, et al.* Giant optical anisotropy in transition metal dichalcogenides for next-generation photonics. *Nature communications* 2021, **12**(1): 1-8.

2. Norden BJTJoPC. Linear and circular dichroism of polymeric pseudoisocyanine. *The Journal of Physical Chemistry* 1977, **81**(2): 151-159.

3. Weber MF, Stover CA, Gilbert LR, Nevitt TJ, Ouderkirk AJJS. Giant birefringent optics in multilayer polymer mirrors. *Science* 2000, **287**(5462): 2451-2456.

4. Nicholls LH, Rodríguez-Fortuño FJ, Nasir ME, Córdova-Castro RM, Olivier N, Wurtz GA, *et al.* Ultrafast synthesis and switching of light polarization in nonlinear anisotropic metamaterials. *Nature Photonics* 2017, **11**(10): 628-633.

5. Mao N, Tang J, Xie L, Wu J, Han B, Lin J, *et al.* Optical anisotropy of black phosphorus in the visible regime. *Journal of the American Chemical Society* 2016, **138**(1): 300-305.

6. Wang YY, Zhou JD, Jiang J, Yin TT, Yin ZX, Liu Z, *et al.* In-plane optical anisotropy in ReS 2 flakes determined by angle-resolved polarized optical contrast spectroscopy. *Nanoscale* 2019, **11**(42): 20199-20205.

7. Kats MA, Genevet P, Aoust G, Yu N, Blanchard R, Aieta F, *et al.* Giant birefringence in optical antenna arrays with widely tailorable optical anisotropy. *Proceedings of the National Academy of Sciences* 2012, **109**(31): 12364-12368.

8. Huang B, Clark G, Navarro-Moratalla E, Klein DR, Cheng R, Seyler KL, *et al.* Layer-dependent ferromagnetism in a van der Waals crystal down to the monolayer limit. *Nature* 2017, **546**(7657): 270-273.

9. Gong C, Li L, Li Z, Ji H, Stern A, Xia Y, *et al.* Discovery of intrinsic ferromagnetism in two-dimensional van der Waals crystals. *Nature* 2017, **546**(7657): 265-269.

10. Lançon D, Walker H, Ressouche E, Ouladdiaf B, Rule K, McIntyre G, *et al.* Magnetic structure and magnon dynamics of the quasi-two-dimensional antiferromagnet FePS 3. *Physical Review B* 2016, **94**(21): 214407.

11. Lançon D, Ewings R, Guidi T, Formisano F, Wildes AJPRB. Magnetic exchange parameters and anisotropy of the quasi-two-dimensional antiferromagnet NiPS 3. *Physical Review B* 2018, **98**(13): 134414.

12. Lee J-U, Lee S, Ryoo JH, Kang S, Kim TY, Kim P, *et al.* Ising-type magnetic ordering in atomically thin FePS3. *Nano letters* 2016, **16**(12): 7433-7438.

13. Wang X, Du K, Liu YYF, Hu P, Zhang J, Zhang Q, *et al.* Raman spectroscopy of atomically thin two-dimensional magnetic iron phosphorus trisulfide (FePS3) crystals. *2D Materials* 2016, **3**(3): 031009.

14. McCreary A, Simpson JR, Mai TT, McMichael RD, Douglas JE, Butch N, *et al.*

Quasi-two-dimensional magnon identification in antiferromagnetic FeP S 3 via magneto-Raman spectroscopy. *Physical Review B* 2020, **101**(6): 064416.

15. Kim K, Lim SY, Lee J-U, Lee S, Kim TY, Park K, *et al.* Suppression of magnetic ordering in XXZ-type antiferromagnetic monolayer NiPS 3. *Nature communications* 2019, **10**(1): 1-9.

16. Sun Z, Yi Y, Song T, Clark G, Huang B, Shan Y, *et al.* Giant nonreciprocal second-harmonic generation from antiferromagnetic bilayer CrI 3. *Nature* 2019, **572**(7770): 497-501.

17. Chu H, Roh CJ, Island JO, Li C, Lee S, Chen J, *et al.* Linear Magnetoelectric Phase in Ultrathin MnPS 3 Probed by Optical Second Harmonic Generation. *Physical review letters* 2020, **124**(2): 027601.

18. Ni Z, Haglund A, Wang H, Xu B, Bernhard C, Mandrus D, *et al.* Imaging the Néel vector switching in the monolayer antiferromagnet MnPSe 3 with strain-controlled Ising order. *Nature Nanotechnology* 2021: 1-6.

19. Le Flem G, Brec R, Ouvard G, Louisy A, Segransan PJJoP, Solids Co. Magnetic interactions in the layer compounds MPX3 (M= Mn, Fe, Ni; X= S, Se). *Journal of Physics* 1982, **43**(5): 455-461.

20. Chittari BL, Park Y, Lee D, Han M, MacDonald AH, Hwang E, *et al.* Electronic and magnetic properties of single-layer m P X 3 metal phosphorous trichalcogenides. *Physical Review B* 2016, **94**(18): 184428.

21. Wildes AR, Simonet V, Ressouche E, Mcintyre GJ, Avdeev M, Suard E, *et al.* Magnetic structure of the quasi-two-dimensional antiferromagnet NiPS 3. *Physical Review B* 2015, **92**(22): 224408.

22. Xie Q-Y, Wu M, Chen L-M, Bai G, Zou W-Q, Wang W, *et al.* Crystallographic and magnetic properties of van der Waals layered FePS3 crystal. *Chinese Physics B* 2019, **28**(5): 056102.

23. Joy P, Vasudevan SJPRB. Magnetism in the layered transition-metal thiophosphates M PS 3 (M= Mn, Fe, and Ni). *Physical Review B* 1992, **46**(9): 5425.

24. Kim SY, Kim TY, Sandilands LJ, Sinn S, Lee M-C, Son J, *et al.* Charge-Spin Correlation in van der Waals Antiferromagnet NiPS 3. *Physical review letters* 2018, **120**(13): 136402.

25. Hwangbo K, Zhang Q, Jiang Q, Wang Y, Fonseca J, Wang C, *et al.* Highly

anisotropic excitons and multiple phonon bound states in a van der Waals antiferromagnetic insulator. *Nature Nanotechnology* 2021, **16**(6): 655-660.

26. Kats MA, Blanchard R, Genevet P, Capasso FJNm. Nanometre optical coatings based on strong interference effects in highly absorbing media. *Nature materials* 2013, **12**(1): 20-24.

27. Jariwala D, Davoyan AR, Tagliabue G, Sherrott MC, Wong J, Atwater HAJNl. Near-unity absorption in van der Waals semiconductors for ultrathin optoelectronics. *Nano letters* 2016, **16**(9): 5482-5487.

28. Zhang H, Abhiraman B, Zhang Q, Miao J, Jo K, Roccasecca S, *et al.* Hybrid exciton-plasmon-polaritons in van der Waals semiconductor gratings. *Nature communications* 2020, **11**(1): 1-9.

29. Zhang X-X, Jiang S, Lee J, Lee C, Mak KF, Shan JJNL. Spin dynamics slowdown near the antiferromagnetic critical point in atomically thin FePS3. *Nano Letters* 2021.

30. Wang X, Cao J, Lu Z, Cohen A, Kitadai H, Li T, *et al.* Spin-induced linear polarization of photoluminescence in antiferromagnetic van der Waals crystals. *Nature Materials* 2021: 1-7.

31. Deng Y, Yu Y, Song Y, Zhang J, Wang NZ, Sun Z, *et al.* Gate-tunable room-temperature ferromagnetism in two-dimensional Fe 3 GeTe 2. *Nature* 2018, **563**(7729): 94-99.

32. Mandziak A, Soria GD, Prieto JE, Prieto P, Granados-Miralles C, Quesada A, *et al.* Tuning the Néel temperature in an antiferromagnet: the case of Ni x Co 1− x O microstructures. *Scientific reports* 2019, **9**(1): 1-8.

33. Eid K, Sheu B, Maksimov O, Stone M, Schiffer P, Samarth NJAPL. Nanoengineered Curie temperature in laterally patterned ferromagnetic semiconductor heterostructures. *Applied Physics Letters* 2005, **86**(15): 152505.

34. Li Q, Yang M, Gong C, Chopdekar RV, N'Diaye AT, Turner J, *et al.* Patterning-induced ferromagnetism of Fe3GeTe2 van der Waals materials beyond room temperature. *Nano letters* 2018, **18**(9): 5974-5980.

35. Yang Y, Liu SC, Wang Y, Long M, Dai CM, Chen S, *et al.* In‐Plane Optical Anisotropy of Low‐Symmetry 2D GeSe. *Advanced Optical Materials* 2019, **7**(4): 1801311.

36. Zhong M, Meng H, Liu S, Yang H, Shen W, Hu C, *et al.* In-Plane Optical and Electrical Anisotropy of 2D Black Arsenic. *ACS nano* 2020.

37. Li S, Opsal J, Chu H, Aspnes DEJJA. Detection and analysis of depolarization artifacts in rotating-compensator polarimeters. *JOSA A* 2001, **18**(2): 426-434.